Biomech Model Mechanobiol
DOI 10.1007/s10237-010-0275-x

ORIGINAL PAPER

Computational modeling of growth: systemic and pulmonary hypertension in the heart

M. K. Rausch · A. Dam · S. Göktepe · O. J. Abilez · E. Kuhl

Received: 6 August 2010 / Accepted: 25 November 2010

Abstract We introduce a novel constitutive model for growing soft biological tissue and study its performance in two characteristic cases of mechanically induced wall thickening of the heart. We adopt the concept of an incompatible growth configuration introducing the multiplicative decomposition of the deformation gradient into an elastic and a growth part. The key feature of the model is the definition of the evolution equation for the growth tensor which we motivate by pressure-overload-induced sarcomerogenesis. In response to the deposition of sarcomere units on the molecular level, the individual heart muscle cells increase in diameter, and the wall of the heart becomes progressively thicker. We present the underlying constitutive equations and their algorithmic implementation within an implicit nonlinear finite element framework. To demonstrate the features of the proposed approach, we study two classical growth phenomena in the heart: left and right ventricular wall thickening in response to systemic and pulmonary hypertension.

Keywords Biomechanics · Growth · Remodeling · Finite elements · Hypertension · Hypertrophy

M. K. Rausch · A. Dam
Department of Mechanical Engineering, Stanford University,
496 Lomita Mall, Stanford, CA 94305, USA
e-mail: mkrausch@stanford.edu

A. Dam
e-mail: antondam@stanford.edu

S. Göktepe
Department of Civil Engineering,
Middle East Technical University, Ankara 06531, Turkey
e-mail: sgoktepe@metu.edu.tr

O. J. Abilez
Departments of Bioengineering and Surgery, Stanford University,
318W Campus Dr., Stanford, CA 94305, USA
e-mail: ojabilez@stanford.edu

E. Kuhl (✉)
Departments of Mechanical Engineering, Bioengineering,
and Cardiothoracic Surgery, Stanford University,
Stanford, CA 94305-4040, USA
e-mail: ekuhl@stanford.edu

1 Introduction

Biological tissue is different from most engineering materials in that it is able to adapt to changes in its mechanical environment (Taber 1995). We can see this remodeling process in skeletal muscle, for example, as a growth in the muscle's cross section in response to increased load during exercise. Similarly, cardiac muscle that experiences elevated stress due to abnormally high blood pressure in the ventricles, the lower chambers of the heart, undergoes transverse thickening, known as cardiac hypertrophy (Göktepe et al. 2010c). Even mild hypertension, if sufficiently prolonged, may induce hypertrophic ventricular growth. One out of four Americans suffers from hypertension of at least this degree (Kumar et al. 2005). On a microscopic scale, hypertrophic wall thickening can be attributed to a parallel addition of sarcomeres, the basic motor units of the muscle cell, associated with an increase in cellular volume and mass (Sawada and Kawamura 1991). Even though muscular growth is initially an adaptive process that normalizes ventricular wall stress and ensures adequate supply of blood to our body, it may progress to heart failure, a maladaptive condition associated with high morbidity and mortality (Berne and Levy 2001).

Numerous clinical conditions have been correlated with elevated left ventricular blood pressure. However, in most cases increased systemic resistance due to outflow obstruction is the cause (Emmanouilides et al. 1994). Among other

Published online: 25 December 2010

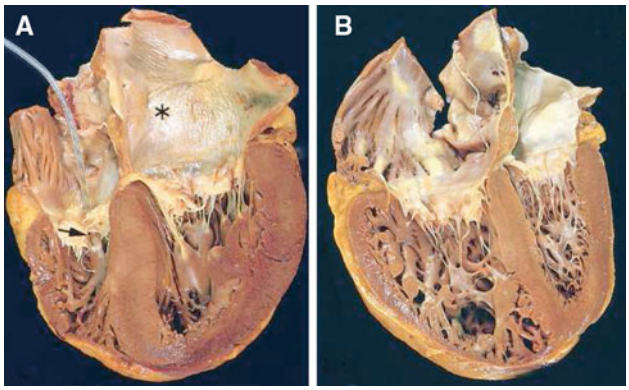

Fig. 1 Systemic and pulmonary hypertension in the heart. Systemic, or left-sided, hypertension is characterized through concentric thickening of the left ventricular wall causing a reduction in cavity volume, *left*. Pulmonary, or right-sided, hypertension is characterized through a significantly dilated right ventricle with a thickened free wall, *right*. The shape of the left ventricle has been distorted by the enlarged right ventricle. The left ventricle is shown on the *right*, the right ventricle is shown on the *left*, in these apical four-chamber views of the heart. Reprinted with permission (Kumar et al. 2005)

reasons, aortic stenosis, a partial occlusion of the outflow tract of the left ventricle, and a narrowing of the downstream blood vessels, the arteries, contribute to the increased resistance to blood flow. Subsequently, the left heart undergoes a series of changes initially compensating for the higher mechanical demands (Hunter and Chien 1999). Under chronic hypertension, however, an increased left ventricular wall thickness may result in impaired perfusion of the cardiac tissue, increased stiffness and, as a consequence, a reduction in cardiac function (Opie 2003), see Fig. 1, left. In addition, secondary to left ventricular changes, enlargement of the left atrium, the upper chamber on the left side of the heart, may corrupt proper signal conduction and result in uncoordinated left atrial and ventricular contraction. If untreated, the maladaptive response of the left heart to hypertension may lead to congestive heart failure and consequently death (Libby et al. 2007).

The study of the right side of the heart is a relatively young field (Haddad et al. 2008). Although it has in principle the same function as the left side, that is to pump blood to the downstream tissue, its appearance is much different. Since the right heart has to overcome a significantly smaller pressure gradient when pumping blood to the lungs, its wall thickness is smaller than the thickness of the left side (Han et al. 2007). In addition, its geometry deviates from an ellipsoid and has been described as crescent shaped in cross section. These differences make the right side more compliant than the left ventricle and more prone to geometric alterations in response to hypertension (Voelkel et al. 2006). Increased afterload of the right side of the heart, known as pulmonary hypertension, can have many origins. Often it is secondary, however, to disease in the left ventricle or to disorders of the lung (Weitzenblum 2003). In either case, similarly to the left side under systemic hypertrophy, extensive growth of the right ventricle may lead to heart failure, see Fig. 1, right. Because of the interdependence of both ventricles, hypertrophy in the right side of the heart may also impair left ventricular function (Haddad et al. 2008).

A vast amount of research has been conducted to deepen our understanding of causes, disease progression, disease treatment, and prevention of maladaptive cardiac growth due to elevated blood pressure. Despite these efforts, unfortunately, there still are a large number of patients suffering from the consequences of pathological remodeling of cardiac tissue. The development of computational models as analytical and predictive tools will provide an improved understanding, particularly from a mechanical point of view, and could be essential in reducing the prevalence of hypertensive cardiac growth.

The first model for volumetric growth in biological tissues was introduced about two decades ago (Rodriguez et al. 1994). Adopting ideas from finite strain plasticity (Lee 1969), this model utilizes the concept of an incompatible growth configuration, introducing the multiplicative decomposition of the deformation gradient into an elastic and a growth part (Garikipati 2009; Himpel et al. 2005; Taber 1995). The last decade has seen tremendous efforts to refine this approach and establish continuum theories of finite growth with the ultimate goal to predict growth in different types of tissues (Ben Amar and Goriely 2005; Epstein and Maugin 2000; Lubarda and Hoger 2002; Menzel 2005). While there seems to be a general agreement on the multiplicative decomposition of the deformation gradient, growth theories are still lacking a rigorous approach to appropriately characterize the evolution of the growth tensor. This is partly due to the fact that there is obviously no universal growth law, since different types of tissues grow in different ways. Typical examples are growth of tumors (Ambrosi and Mollica 2002), tendons (Garikipati et al. 2004), vascular tissue (Alastrue et al. 2009; Humphrey 2008; Kuhl et al. 2007; Taber and Humphrey 2001), and the heart (Kroon et al. 2009; Göktepe et al. 2010c).

The main idea of this manuscript is to closely tie the definition of the macroscopic growth tensor and the forces driving its temporal evolution to observations on the microstructural level (Göktepe et al. 2010b). The heart is an excellent model system for this approach since it consists primarily of cardiomyocytes, which are incapable of dividing or self-renewing (Emmanouilides et al. 1994). Accordingly, the number of cells in the heart, approximately 6 billion at birth, remains relatively constant throughout an individual's life time. The shape of these cells, however, may change and adapt to mechanical loading. It does so by the parallel and serial deposition of its basic functional building blocks, the sarcomere units, which themselves tend to be unaffected

by growth maintaining a constant optimal operating length (Kumar et al. 2005).

The advantage of studying growth of the heart, when compared to growth of other soft tissues, is that changes in cell size and sarcomere number are relatively easy to visualize in vitro (Gerdes et al. 1992) and therefore straightforward to manipulate and quantify (Russel et al. 2010; Yoshida et al. 2010). Moreover, it has been demonstrated experimentally that remodeling and cardiomyocyte slippage play a rather insignificant role during cardiac growth (Gerdes et al. 1992). Accordingly, we attribute pathological changes in systemic and pulmonary hypertension exclusively to morphological changes in the cardiomyocytes themselves, neglecting the effects of extracellular matrix remodeling and fiber reorientation (Himpel et al. 2008; Kuhl et al. 2005; Kuhl and Holzapfel 2007). In hypertension, new sarcomeres are added in parallel to existing sarcomere units to form new myofibrils, the number of which may approximately triple, from about 50–100 to 200 per cardiomyocyte, in response to chronically elevated pressure levels. Accordingly, the individual cardiomyocytes increase in diameter, from approximately 15–40 μm (Kumar et al. 2005), and the wall thickness can increase from 1 to 3 cm in the left ventricle (Maron and McKenna 2003), and from 0.5 to 1.5 cm in the right ventricle (Voelkel et al. 2006).

This manuscript is organized as follows. In Sect. 2, we briefly revisit the modeling of biological growth. In particular, we present a novel constitutive model for growth in anisotropic soft biological tissues and illustrate its algorithmic implementation within an implicit nonlinear finite element setting. In Sect. 4, we demonstrate the features of the proposed growth model in systemic and pulmonary hypertension associated with left- and right-sided heart failure. Finally, we compare the results to pathological observations and discuss potential future directions in Sect. 5.

2 Continuum modeling of cardiac growth

In this section, we illustrate the governing equations of stress-induced cardiac growth. We briefly summarize the kinematic equations, the equilibrium equation, and the constitutive equations.

2.1 Kinematics of hypertensive growth

To characterize growth, we adopt the multiplicative decomposition of deformation gradient $\boldsymbol{F}$ into an elastic part $\boldsymbol{F}^{\mathrm{e}}$ and a growth part $\boldsymbol{F}^{\mathrm{g}}$ (Rodriguez et al. 1994),

$$\boldsymbol{F} = \boldsymbol{F}^{\mathrm{e}} \cdot \boldsymbol{F}^{\mathrm{g}} \qquad \text{with} \qquad \boldsymbol{F} = \nabla_{\boldsymbol{X}} \boldsymbol{\varphi}, \tag{1}$$

a concept that was first proposed in the context of finite elasto-plasticity (Lee 1969). Herein, $\boldsymbol{\varphi}$ is the deformation map between the undeformed and the deformed configuration

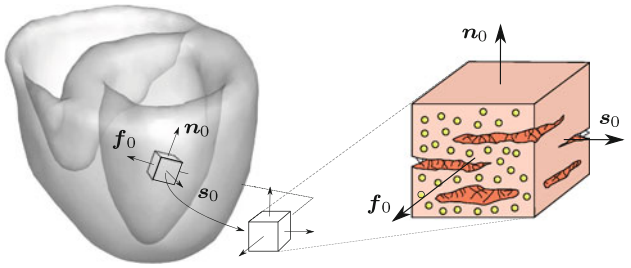

Fig. 2 Characteristic orthotropic architecture of the myocardium made up of cardiac muscle fibers that are arranged in layers of sheets (Harrington et al. 2005). The orthogonal unit vectors $\boldsymbol{f}_0$ and $\boldsymbol{s}_0$ indicate the fiber and sheet directions in the undeformed configuration. The sheet plane unit normal $\boldsymbol{n}_0$ is orthogonal to the both by its definition $\boldsymbol{n}_0 := [\boldsymbol{f}_0 \times \boldsymbol{s}_0]/|\boldsymbol{f}_0 \times \boldsymbol{s}_0|$, (Holzapfel and Ogden 2009; Göktepe et al. 2010a)

and $\nabla_{\boldsymbol{X}}$ denotes its spatial gradient with respect to the undeformed coordinates $\boldsymbol{X}$. Motivated by physiological observations during hypertrophic wall thickening, we introduce a single scalar-valued growth multiplier ϑ, which reflects the parallel deposition of sarcomeres associated with transversely isotropic cardiomyocyte growth on the molecular level (Göktepe et al. 2010b). The growth tensor $\boldsymbol{F}^{\mathrm{g}}$ can thus be expressed as a simple rank-one update of the identity tensor.

$$\boldsymbol{F}^{\mathrm{g}} = \boldsymbol{I} + [\,\vartheta - 1\,]\, \boldsymbol{s}_0 \otimes \boldsymbol{s}_0 \tag{2}$$

We adopt the concept of myocardial sheets (Harrington et al. 2005) in which the individual muscle fibers are arranged in layers, resulting in a locally orthotropic material characterization (Holzapfel and Ogden 2009; Göktepe et al. 2010a) as illustrated in Fig. 2. With the common understanding that the sheet vector $\boldsymbol{s}_0$ is pointing approximately in the radial direction, this form of cardiac growth is directly associated with ventricular wall thickening. The corresponding Jacobians $J = J^{\mathrm{e}}\, J^{\mathrm{g}}$ follow accordingly with $J = \det(\boldsymbol{F})$, $J^{\mathrm{e}} = \det(\boldsymbol{F}^{\mathrm{e}})$ and $J^{\mathrm{g}} = \det(\boldsymbol{F}^{\mathrm{g}}) = \vartheta$. With the definition of the growth tensor (2), we can immediately extract the elastic part of the deformation gradient $\boldsymbol{F}^{\mathrm{e}} = \boldsymbol{F} \cdot \boldsymbol{F}^{\mathrm{g}\,-1}$ which will be essential to characterize the elastically deformed fiber and sheet directions $\boldsymbol{f}^{\mathrm{e}} = \boldsymbol{F}^{\mathrm{e}} \cdot \boldsymbol{f}_0$ and $\boldsymbol{s}^{\mathrm{e}} = \boldsymbol{F}^{\mathrm{e}} \cdot \boldsymbol{s}_0$ as illustrated in Fig. 2. We can then introduce the left Cauchy Green or Finger tensor $\boldsymbol{b}$ and its elastic counterpart $\boldsymbol{b}^{\mathrm{e}}$

$$\boldsymbol{b} = \boldsymbol{F} \cdot \boldsymbol{G}^{-1} \cdot \boldsymbol{F}^{\mathrm{t}} \qquad \boldsymbol{b}^{\mathrm{e}} = \boldsymbol{F}^{\mathrm{e}} \cdot \boldsymbol{G}^{\mathrm{e}-1} \cdot \boldsymbol{F}^{\mathrm{e}\,\mathrm{t}} \tag{3}$$

as the push forward of the inverse material metric $\boldsymbol{G}^{-1}$ and the inverse intermediate metric $\boldsymbol{G}^{\mathrm{e}-1}$, respectively.

2.2 Equilibrium equation of hypertensive growth

In the absence of transient terms and external forces, the balance of linear momentum can be expressed in the following reduced format,

$$\operatorname{div}(\boldsymbol{\sigma}) = \mathbf{0} \tag{4}$$

where $\operatorname{div}(\boldsymbol{\sigma})$ denotes the divergence of the total Cauchy stress $\boldsymbol{\sigma}$ with respect to the spatial position $\boldsymbol{x}$. Experimental and clinical studies suggest that hypertrophic wall thickening is primarily a response to elevated systolic stresses (Kumar et al. 2005). While clinical approaches typically model the difference between systolic and diastolic stresses through increasing the elastic material parameters (Itoh et al. 2009; Krishnamurthy et al. 2009), we will adopt a more mechanical approach and express the total Cauchy stress

$$\boldsymbol{\sigma} = \boldsymbol{\sigma}^{\text{pas}} + \boldsymbol{\sigma}^{\text{act}} \tag{5}$$

as the sum of passive and active contributions (Guccione and McCulloch 1993; Böl et al. 2009; Göktepe and Kuhl 2010). Both will be introduced constitutively in the sequel along with the constitutive definition of the growth multiplier ϑ.

2.3 Constitutive equations of hypertensive growth

To constitutively define the passive stress $\boldsymbol{\sigma}^{\text{pas}}$, we introduce the following Helmholtz free energy function

$$\psi^{\text{pas}} = \psi_J + \psi_1 + \psi_{\text{f}} + \psi_{\text{s}} + \psi_{\text{fs}} \tag{6}$$

motivated by a recently proposed approach for orthotropic cardiac tissue (Göktepe et al. 2010a; Holzapfel and Ogden 2009). It consists of two isotropic and three anisotropic contributions

$$\begin{aligned}
\psi_J &= \kappa \quad [J^{\text{e}} - \ln(J^{\text{e}}) - 1] && J^{\text{e}} = \det(\boldsymbol{F}^{\text{e}}) \\
\psi_1 &= \frac{a}{2b} \quad \exp(b[I_1^{\text{e}} - 3]) && I_1^{\text{e}} = \boldsymbol{g} : \boldsymbol{b}^{\text{e}} \\
\psi_{\text{f}} &= \frac{a_{\text{f}}}{2b_{\text{f}}} [\exp(b_{\text{f}}[I_{\text{f}}^{\text{e}} - 1]^2) - 1] && I_{\text{f}}^{\text{e}} = \boldsymbol{g} : [\boldsymbol{f}^{\text{e}} \otimes \boldsymbol{f}^{\text{e}}] \\
\psi_{\text{s}} &= \frac{a_{\text{s}}}{2b_{\text{s}}} [\exp(b_{\text{s}}[I_{\text{s}}^{\text{e}} - 1]^2) - 1] && I_{\text{s}}^{\text{e}} = \boldsymbol{g} : [\boldsymbol{s}^{\text{e}} \otimes \boldsymbol{s}^{\text{e}}] \\
\psi_{\text{fs}} &= \frac{a_{\text{fs}}}{2b_{\text{fs}}} [\exp(b_{\text{fs}}\, I_{\text{fs}}^{\text{e}\,2}) - 1] && I_{\text{fs}}^{\text{e}} = \boldsymbol{g} : [\boldsymbol{f}^{\text{e}} \otimes \boldsymbol{s}^{\text{e}}]^{\text{sym}}
\end{aligned} \tag{7}$$

parameterized in terms of five elastic invariants J^{e}, I_1^{e}, I_{f}^{e}, I_{s}^{e}, and I_{fs}^{e}, weighted by the bulk modulus κ and the four sets of parameters a and b. Using standard arguments of thermodynamics, the passive Kirchhoff stress $\boldsymbol{\tau}^{\text{pas}} = J\,\boldsymbol{\sigma}^{\text{pas}}$ then follows naturally as the derivative of the Helmholtz free energy ψ^{pas} with respect to the covariant spatial metric $\boldsymbol{g}$,

$$\begin{aligned}
\boldsymbol{\tau}^{\text{pas}} = 2\frac{\partial \psi^{\text{pas}}}{\partial \boldsymbol{g}} = \;& \kappa \quad [\,J^{\text{e}} - 1\,]\,\boldsymbol{g}^{-1} + 2\,\psi_1'\boldsymbol{b}^{\text{e}} \\
& + 2\,\psi_{\text{f}}' \quad \boldsymbol{f}^{\text{e}} \otimes \boldsymbol{f}^{\text{e}} \quad + 2\,\psi_{\text{s}}'\,\boldsymbol{s}^{\text{e}} \otimes \boldsymbol{s}^{\text{e}} \\
& + 2\,\psi_{\text{fs}}'\,[\boldsymbol{f}^{\text{e}} \otimes \boldsymbol{s}^{\text{e}}]^{\text{sym}}
\end{aligned} \tag{8}$$

in terms of two isotropic and three anisotropic contributions with

$$\begin{aligned}
\psi_1' &= a \qquad \tfrac{1}{2}\ \exp(b\ [I_1^{\text{e}} - 3]) \\
\psi_{\text{f}}' &= a_{\text{f}}\,[I_{\text{f}}^{\text{e}} - 1]\,\exp(b_{\text{f}}\,[I_{\text{f}}^{\text{e}} - 1]^2) \\
\psi_{\text{s}}' &= a_{\text{s}}\,[I_{\text{s}}^{\text{e}} - 1]\,\exp(b_{\text{s}}\,[I_{\text{s}}^{\text{e}} - 1]^2) \\
\psi_{\text{fs}}' &= a_{\text{fs}}\ I_{\text{fs}}^{\text{e}} \qquad \exp(b_{\text{fs}}\ I_{\text{fs}}^{\text{e}\,2}).
\end{aligned} \tag{9}$$

We assume that the active stress $\boldsymbol{\tau}^{\text{act}} = J\,\boldsymbol{\sigma}^{\text{act}}$ is acting exclusively along the fiber direction $\boldsymbol{f}^{\text{e}}$,

$$\boldsymbol{\tau}^{\text{act}} = T^{\text{act}}(I_{\text{f}}^{\text{e}}, c_{\text{Ca}})\ \boldsymbol{f}^{\text{e}} \otimes \boldsymbol{f}^{\text{e}} \tag{10}$$

and that its magnitude T^{act} is dependent on the intracellular calcium concentration c_{Ca} and on the current sarcomere length $l = \sqrt{I_{\text{f}}^{\text{e}}}\,L$, where L is the sarcomere resting length in the underformed configuration (Guccione and McCulloch 1993; Guccione et al. 2001). In particular, we choose the following formulation,

$$T^{\text{act}} = T^{\max}\,\frac{{c_{\text{Ca}}}^2}{{c_{\text{Ca}}}^2 + \tilde{c}_{\text{Ca}}^{\,2}} \quad \text{with} \quad \tilde{c}_{\text{Ca}} = \tilde{c}_{\text{Ca}}(I_{\text{f}}^{\text{e}}) \tag{11}$$

where $T^{\max}$ is the maximum isometric tension found at the maximum intracellular calcium concentration $c_{\text{Ca}}^{\max}$, and $\tilde{c}_{\text{Ca}}$ is the length-dependent calcium concentration. We modify its original definition $\tilde{c}_{\text{Ca}}{}^2 = 1/[\exp(\beta[l - l_0]) - 1]c_{\text{Ca}}^{\max 2}$ proposed in (Guccione and McCulloch 1993), to obtain a smooth dependence of the active stress on the current sarcomere length $l = \sqrt{I_{\text{f}}^{\text{e}}}\,L$.

$$\tilde{c}_{\text{Ca}}^2 = \left[1/\exp(-\exp(-\xi\,[l - l_0])) - 1\right] c_{\text{Ca}}^{\max 2} \tag{12}$$

The parameters ξ and l_0 characterize the slope of the Starling curve and the optimal sarcomere operating length, respectively. Since we are not interested in calcium dynamics but rather in the state of maximum systolic stress, we assume optimal calcium conditions (Guccione et al. 2001), $c_{\text{Ca}}^{\max} = c_{\text{Ca}}$, such that Eq. (11) reduces to the following simplified expression illustrated in Fig. 3.

$$T^{\text{act}} = T^{\max} \exp(-\exp(-\xi\,[l - l_0])) \tag{13}$$

Motivated by pathological observations, we introduce a stress-driven evolution equation for concentric hypertrophic growth

$$\dot{\vartheta} = k(\vartheta)\,\phi(\boldsymbol{\tau}) \tag{14}$$

in terms of the growth scaling function $k(\vartheta)$ and the growth criterion $\phi(\boldsymbol{\tau})$ with

$$k = \frac{1}{\tau_\vartheta}\left[\frac{\vartheta^{\max} - \vartheta}{\vartheta^{\max} - 1}\right]^\gamma \quad \text{and} \quad \phi = \operatorname{tr}(\boldsymbol{\tau}) - p^{\text{crit}}. \tag{15}$$

Herein, τ_ϑ denotes the adaptation speed, $\vartheta^{\max}$ is the area fraction of maximum parallel sarcomere deposition, and γ

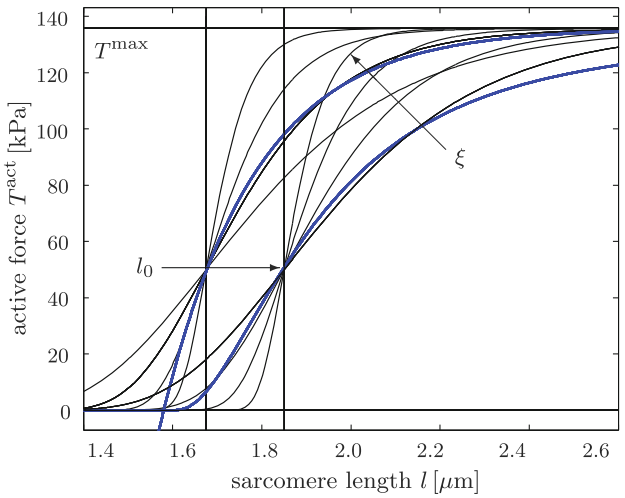

Fig. 3 Active force versus sarcomere length. According to Starling's law, the active force increases with increased sarcomere length. The *thin lines* illustrate our smooth active force relation, $T^{\text{act}} = T^{\max} \exp(-\exp(-\xi[l - l_0]))$. Increasing the slope parameter ξ increases the slope of the active force curve. Increasing the optimal sarcomere operating length shifts the active force curve to the right. The *thick lines* in the background illustrate the original active force relation proposed in the literature (Guccione and McCulloch 1993; Guccione et al. 2001)

is the degree of sarcomere deposition nonlinearity (Göktepe et al. 2010b; Lubarda and Hoger 2002). Following thermodynamical considerations, we choose the physiological overstress $\text{tr}(\boldsymbol{\tau}) - p^{\text{crit}}$, i.e., the difference between the trace of the Kirchhoff stress $\text{tr}(\boldsymbol{\tau}) = \boldsymbol{\tau} : \boldsymbol{g}$ and the baseline pressure level p^{crit} as the driving force for growth (Epstein and Maugin 2000; Himpel et al. 2005).

Remark 1 (Growth and incompressibility) In the kinematic setting of finite growth, incompressibility could be taken into account by penalizing the total volume change. However, this approach does not seem justified for soft tissues that may undergo considerable volume changes during growth. In particular in the context of hypertrophic wall thickening, it seems more appropriate to impose incompressibility (Schmid et al. 2010) or quasi-incompressibility (Himpel et al. 2005) on the elastic part of the deformation. Rather than requiring strict incompressibility as we have recently proposed (Göktepe et al. 2010a), in this manuscript, we will impose quasi-incompressibility through a sufficiently large bulk modulus κ in the volumetric part of the free energy. Quasi-incompressibility might be justified for cardiac muscle which has been reported to undergo volume changes of up to 5–10% attributed to the vascular network that constitutes about 10–20% of the total muscle volume (Yin et al. 1996).

Remark 2 (Growth and open systems) In the present approach, we characterize the growth process through a single growing solid phase and essentially neglect the biochemical origin of the growing material. In a thermodynamic sense, this implies that we are modeling the growing tissue as an open system that is allowed to increase its mass (Kuhl and Steinmann 2003a,b; Kuhl et al. 2003). This mass change gains a more illustrative biochemical interpretation in the context of mixture theories (Garikipati et al. 2004; Humphrey and Rajagopal 2002).

3 Computational modeling of cardiac growth

In this section, we will illustrate the algorithmic realization of finite growth within an incremental iterative nonlinear finite element setting. In particular, we illustrate the linearizations required for the local and global Newton iterations and summarize the algorithm in an illustrative flowchart.

3.1 Local Newton iteration: iterative update of growth multiplier

Our goal is to determine the current growth multiplier ϑ for a given deformation state $\boldsymbol{F}$ at time t, and a given growth multiplier ϑ_{n} at the end of the previous time step t_{n}. We introduce the following finite difference approximation of the first-order material time derivative, $\dot{\vartheta} = [\,\vartheta - \vartheta_{\text{n}}\,]/\Delta t$ where $\Delta t = t - t_{\text{n}} > 0$ denotes the current time increment. In the spirit of implicit time stepping schemes, we now reformulate the evolution equation (14) with the help of this finite difference approximation, introducing the discrete residual R in terms of the unknown growth multiplier ϑ.

$$\mathsf{R} = \vartheta - \vartheta_{\text{n}} - \frac{1}{\tau_\vartheta}\left[\frac{\vartheta^{\max} - \vartheta}{\vartheta^{\max} - 1}\right]^{\gamma}\left[\,\text{tr}(\boldsymbol{\tau}) - p^{\text{crit}}\right]\Delta t \doteq 0 \qquad (16)$$

Within each local Newton iteration, we can then express the iterative update of the growth multiplier $\vartheta \leftarrow \vartheta - \mathsf{R}\,/\,\mathsf{K}$ in terms of the discrete residual R and its linearization K.

$$\mathsf{K} = \frac{\mathrm{d}\mathsf{R}}{\mathrm{d}\vartheta} = 1 - \left[k\,\frac{\partial \phi}{\partial \vartheta} + \phi\,\frac{\partial k}{\partial \vartheta}\right]\Delta t \qquad (17)$$

The discrete sensitivities in the above equation take the following explicit representations,

$$\frac{\partial \phi}{\partial \vartheta} = \frac{\partial \boldsymbol{\tau}}{\partial \vartheta} : \boldsymbol{g} \quad \text{and} \quad \frac{\partial k}{\partial \vartheta} = -\frac{\gamma}{[\vartheta^{\max} - \vartheta]}\,k. \qquad (18)$$

3.2 Global Newton iteration: consistent linearization of hypertensive growth

Upon convergence of ϑ, we can successively update the growth tensor $\boldsymbol{F}^{\text{g}} = \boldsymbol{I} + [\,\vartheta - 1\,]\,\boldsymbol{s}_0 \otimes \boldsymbol{s}_0$ from Eq. (2), the elastic tensor $\boldsymbol{F}^{\text{e}} = \boldsymbol{F} \cdot \boldsymbol{F}^{\text{g}\,-1}$ from Eq. (1), and the Kirchhoff stress $\boldsymbol{\tau} = 2\,\partial\psi/\partial\boldsymbol{g}$ from Eq. (5), to finally evaluate the global equilibrium Eq. (4). For its solution, we propose a global Newton iteration based on the consistent algorithmic linearization of the Kirchhoff stress $\boldsymbol{\tau}$ with respect to

the spatial metric $\boldsymbol{g}$ introducing the Eulerian constitutive moduli $\mathbf{e}$.

$$\mathbf{e} = 2\,\frac{\mathrm{d}\boldsymbol{\tau}}{\mathrm{d}\boldsymbol{g}} = 2\,\frac{\partial \boldsymbol{\tau}}{\partial \boldsymbol{g}}\bigg|_{\vartheta} + 2\,\frac{\partial \boldsymbol{\tau}}{\partial \vartheta}\bigg|_{\boldsymbol{g}} \otimes \frac{\partial \vartheta}{\partial \boldsymbol{g}} = \mathbf{e}^{\mathrm{e}} + \mathbf{e}^{\mathrm{g}} \tag{19}$$

The first term represents the classical elastic Eulerian moduli

$$\mathbf{e}^{\mathrm{e}} = 2\frac{\partial \boldsymbol{\tau}}{\partial \boldsymbol{g}} = \mathbf{e}^{\mathrm{pas}} + \mathbf{e}^{\mathrm{act}} \tag{20}$$

which can be expressed as the sum of passive

$$\begin{aligned} \mathbf{e}^{\mathrm{pas}} = 2\frac{\partial \boldsymbol{\tau}^{\mathrm{pas}}}{\partial \boldsymbol{g}} = {} & J^{\mathrm{e}}\ \kappa\ \ \boldsymbol{g}^{-1}\otimes\boldsymbol{g}^{-1} + 2\kappa\,[J^{\mathrm{e}}-1]\,\partial_{\boldsymbol{g}}\boldsymbol{g}^{-1} \\ & + 4\ \ \psi_1''\ \ \ \ \boldsymbol{b}^{\mathrm{e}}\ \ \ \ \otimes\ \ \boldsymbol{b}^{\mathrm{e}} \\ & + 4\ \ \psi_{\mathrm{f}}''\ \ \boldsymbol{f}^{\mathrm{e}}\otimes\boldsymbol{f}^{\mathrm{e}}\ \ \otimes\ \ \boldsymbol{f}^{\mathrm{e}}\otimes\ \ \boldsymbol{f}^{\mathrm{e}} \\ & + 4\ \ \psi_{\mathrm{s}}''\ \ \boldsymbol{s}^{\mathrm{e}}\otimes\boldsymbol{s}^{\mathrm{e}}\ \ \otimes\ \ \boldsymbol{s}^{\mathrm{e}}\otimes\ \ \boldsymbol{s}^{\mathrm{e}} \\ & + 4\ \ \psi_{\mathrm{fs}}''\,[\,\boldsymbol{f}^{\mathrm{e}}\otimes\boldsymbol{s}^{\mathrm{e}}\,]^{\mathrm{sym}}\otimes[\,\boldsymbol{f}^{\mathrm{e}}\otimes\ \ \boldsymbol{s}^{\mathrm{e}}]^{\mathrm{sym}} \end{aligned} \tag{21}$$

and active contributions.

$$\mathbf{e}^{\mathrm{act}} = 2\frac{\partial \boldsymbol{\tau}^{\mathrm{act}}}{\partial \boldsymbol{g}} = 2\,T^{\mathrm{act}\prime}\,\boldsymbol{f}^{\mathrm{e}}\otimes\boldsymbol{f}^{\mathrm{e}}\otimes\boldsymbol{f}^{\mathrm{e}}\otimes\boldsymbol{f}^{\mathrm{e}} \tag{22}$$

The derivatives in Eq. (21) and (22) take the following explicit representations

$$\begin{aligned} \psi_1'' &= a && \tfrac{1}{2}b && \exp\left(b\,[I_1^{\mathrm{e}}-3]\right) \\ \psi_{\mathrm{f}}'' &= a_{\mathrm{f}} && [\,1+2\,b_{\mathrm{f}}[I_{\mathrm{f}}^{\mathrm{e}}-1]^2] && \exp(b_{\mathrm{f}}\,[I_{\mathrm{f}}^{\mathrm{e}}-1]^2) \\ \psi_{\mathrm{s}}'' &= a_{\mathrm{s}} && [\,1+2\,b_{\mathrm{s}}[I_{\mathrm{s}}^{\mathrm{e}}-1]^2] && \exp(b_{\mathrm{s}}\,[I_{\mathrm{s}}^{\mathrm{e}}-1]^2) \\ \psi_{\mathrm{fs}}'' &= a_{\mathrm{fs}} && [\,1+2\,b_{\mathrm{fs}}\,I_{\mathrm{fs}}^{\mathrm{e}\,2}\,] && \exp(b_{\mathrm{fs}}I_{\mathrm{fs}}^{\mathrm{e}\,2}). \end{aligned} \tag{23}$$

and, for the case of $c_{\mathrm{Ca}} = c_{\mathrm{Ca}}^{\max}$ considered herein,

$$T^{\mathrm{act}\prime} = \frac{1}{2}\,T^{\mathrm{act}}\,\xi\,\exp(-\xi\,[l-l_0])\,L^2/l. \tag{24}$$

The second term in the overall Eulerian moduli (19) reflects the effects of hypertensive growth and is only active in the inelastic case.

$$\mathbf{e}^{\mathrm{g}} = 2\frac{\partial \boldsymbol{\tau}}{\partial \vartheta}\otimes\frac{\partial \vartheta}{\partial \boldsymbol{g}} \tag{25}$$

It consists of the linearization of the Kirchhoff stress $\boldsymbol{\tau}$ with respect to the growth multiplier ϑ, a term that obviously depends on the particular choice of the constitutive equation.

$$\begin{aligned} \frac{\partial \boldsymbol{\tau}}{\partial \vartheta} = {} & \frac{1}{\vartheta}\,J^{\mathrm{e}}\kappa\,\boldsymbol{g}^{-1} \\ & - \frac{4}{\vartheta}\,[\,\psi_1' I_{\mathrm{s}}^{\mathrm{e}}\boldsymbol{b}^{\mathrm{e}} + [\,\psi_{\mathrm{s}}' I_{\mathrm{s}}^{\mathrm{e}}\ + \psi_{\mathrm{s}} + \psi_1]\boldsymbol{s}^{\mathrm{e}}\otimes\boldsymbol{s}^{\mathrm{e}} \\ & \qquad + [\,\psi_{\mathrm{fs}}' I_{\mathrm{fs}}^{\mathrm{e}} + \psi_{\mathrm{fs}}][\boldsymbol{f}^{\mathrm{e}}\otimes\boldsymbol{s}^{\mathrm{e}}]^{\mathrm{sym}}] \end{aligned} \tag{26}$$

Table 1 Algorithmic treatment of stress-driven transversely isotropic growth through parallel sarcomere deposition

given $\boldsymbol{F}$ and ϑ_{n}	
initialize $\vartheta \leftarrow \vartheta_{\mathrm{n}}$	
local Newton iteration	
calculate growth tensor $\boldsymbol{F}^{\mathrm{g}} = \boldsymbol{I} + [\,\vartheta - 1\,]\,\boldsymbol{s}_0\otimes\boldsymbol{s}_0$	(2)
calculate elastic tensor $\boldsymbol{F}^{\mathrm{e}} = \boldsymbol{F}\cdot\boldsymbol{F}^{\mathrm{g}\,-1}$	(1)
calculate elastic Finger tensor $\boldsymbol{b}^{\mathrm{e}} = \boldsymbol{F}^{\mathrm{e}}\cdot\boldsymbol{F}^{\mathrm{e}\,\mathrm{t}}$	(3)
calculate Kirchhoff stress $\boldsymbol{\tau} = \boldsymbol{\tau}^{\mathrm{pas}} + \boldsymbol{\tau}^{\mathrm{act}}$	(5),(8),(10)
check growth criterion $\phi = \mathrm{tr}(\boldsymbol{\tau}) - p^{\mathrm{crit}} \geq 0$?	(15.1)
calculate growth function $k(\vartheta)$	(15.2)
calculate residual $\mathsf{R} = \vartheta - \vartheta_{\mathrm{n}} - k\,\phi\Delta t$	(16)
calculate tangent $\mathsf{K} = \partial\mathsf{R}\,/\,\partial\vartheta$	(17),(18)
update growth multiplier $\vartheta \leftarrow \vartheta - \mathsf{R}\,/\,\mathsf{K}$	
check convergence $\mathsf{R} \leq \mathrm{tol}$?	
calculate Eulerian moduli $\mathbf{e}$	(19)-(27)

This term is multiplied with the consistent algorithmic linearization of the converged growth multiplier ϑ with respect to the spatial metric $\boldsymbol{g}$.

$$\frac{\partial \vartheta}{\partial \boldsymbol{g}} = \frac{k}{\mathsf{K}}\,\Delta t\left[\frac{1}{2}\,\boldsymbol{e}^{\mathrm{e}} : \boldsymbol{g} + \boldsymbol{\tau}\right] \tag{27}$$

We would like to point out that only very specific stress-driven isotropic growth formulations actually yield a symmetric tangent operator, while this formulation obviously does not, see Göktepe et al. (2010c) for details.

3.3 Algorithmic treatment of hypertensive growth

Table 1 illustrates the algorithmic treatment of stress-driven transversely isotropic growth through parallel sarcomere deposition.

4 Examples

To explore the features of the proposed growth model, we study the effects of systemic and pulmonary hypertension in a generic biventricular heart geometry (Göktepe et al. 2010a). In this idealized prototype model, the left and right ventricles are represented through two truncated ellipsoids with heights of 70 and 60 mm and radii of 30 and 51 mm, respectively. They are connected such that the right ventricle blends smoothly into the left ventricle from apex to base, see Fig. 4. The left ventricle that pumps oxygenated blood into the body operates at a higher pressure and typically has a larger wall thickness than the right ventricle that pumps deoxygenated blood into the lungs. We therefore assume an initial left ventricular wall thickness of 12 mm, while the right ventricular wall is assumed to be 6 mm thick. The

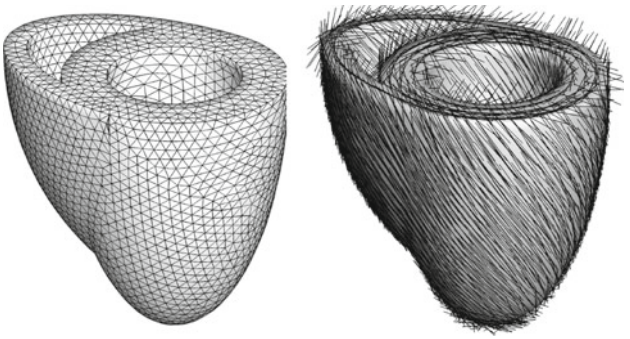

Fig. 4 Generic biventricular heart model generated from two truncated ellipsoids, with heights of 70 and 60 mm, radii of 30 and 51 mm, and wall thicknesses of 12 and 6 mm, respectively (Göktepe and Kuhl 2010; Göktepe et al. 2010a). The generic heart is discretized with 33,713 linear tetrahedral elements connected at 6,718 nodes, *left*. Fiber orientations vary transmurally from $-70°$ in the epicardium, the outer layer, to $+70°$ in the endocardium, the inner layer, *right*

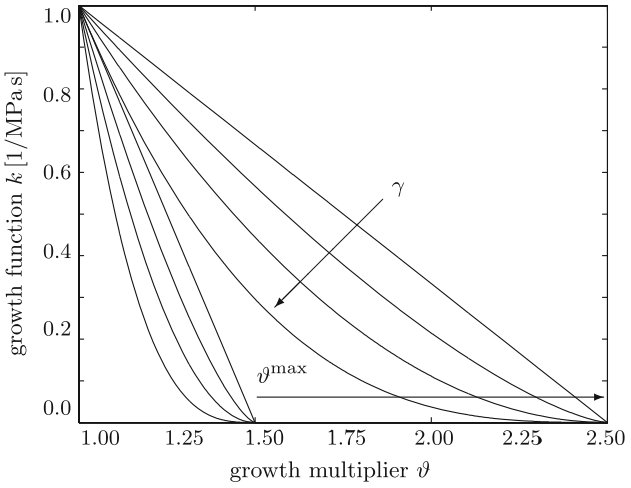

Fig. 5 Growth function versus growth multiplier. The growth function $k = \left[\left[\vartheta^{\max} - \vartheta\right] / \left[\vartheta^{\max} - 1\right]\right]^{\gamma} / \tau_{\vartheta}$ decreases gradually as the growth multiplier ϑ reaches the maximum parallel sarcomere deposition $\vartheta^{\max}$. Increasing the degree of growth nonlinearity γ changes the rate of parallel sarcomere deposition. Increasing the maximum parallel sarcomere deposition $\vartheta^{\max}$ increases the amount of potential growth

generic biventricular heart is discretized with 33,713 linear tetrahedral elements connected at 6,718 nodes. In the healthy heart, cardiomyocytes are arranged helically around the ventricles. We therefore assume the fiber direction $\boldsymbol{f}_0$ to vary transmurally from an inclination of $-70°$ in the epicardium, the outer layer, to $+70°$ in the endocardium, the inner layer, measured with respect to the basal plane, see Fig. 4. For the sake of simplicity, the myocardial sheet directions $\boldsymbol{s}_0$ are assumed be oriented normal to the endocardium and epicardium. The left and right ventricular endocardium are subject to ventricular pressures that are increased linearly, then held constant, and finally decreased linearly back to zero, see Figs. 6 and 9. As baseline values, we assume a left and right ventricular pressure of $p_{\text{LV}} = 100\,\text{mmHg}$ and $p_{\text{RV}} = 20\,\text{mmHg}$, respectively. For the lack of better knowledge, we apply homogeneous Dirichlet boundary conditions to all nodes in the basal plane. In addition, to mimic the boundary conditions imposed by the surrounding tissue, we support all nodes of the epicardium by linear springs with a stiffness of $k = 10^{-3}\,\text{N/mm}$ in the radial and tangential directions. The material parameters for the passive elastic response, $a = 0.000496$, $b = 7.21$, $a_{\text{f}} = 0.0152$, $b_{\text{f}} = 20.42$, $a_{\text{s}} = 0.00328$, $b_{\text{s}} = 11.18$, $a_{\text{fs}} = 0.00066$, and $b_{\text{fs}} = 9.4662$, have been identified using six cyclic simple shear experiments (Dokos et al. 2002) as recently demonstrated (Holzapfel and Ogden 2009; Göktepe et al. 2010a). The bulk modulus is chosen to $\kappa = 2.87\,\text{MPa}$. The material parameters characterizing the active contraction are the maximum isometric tension $T^{\max} = 0.1357\,\text{MPa}$, the sarcomere resting length $L = 1.85\,\mu\text{m}$, the intracellular calcium concentration $c_{\text{Ca}} = 4.35\,\mu\text{mol/L}$, and the maximum intracellular calcium concentration $c_{\text{Ca}}^{\max} = 4.35\,\mu\text{mol/L}$, adopted from the literature (Guccione and McCulloch 1993; Guccione et al. 2001). The slope parameter $\xi = 10\,\mu\text{m}^{-1}$ and the optimal sarcomere operating length $l_0 = 2.00\,\mu\text{m}$ are fit to match the active force curve reported in the literature (Guccione et al. 2001) according to the sensitivity studies reported in Fig. 3. The additional growth parameters are the adaptation speed $\tau_{\vartheta} = 1.0\,\text{MPa s}$, the degree of growth nonlinearity $\gamma = 3.0$, the area fraction of maximum parallel sarcomere deposition $\vartheta^{\max} = 4.0$, and the growth stress $p^{\text{crit}} = 0.08\,\text{MPa}$, which would take the interpretation of the yield stress in the theory of plasticity. The growth parameters are adopted from the recent literature (Göktepe et al. 2010b,c), and their sensitivities are illustrated in Fig. 5. At this point, the choices of the time parameter τ_{ϑ} and the nonlinearity parameter γ are relatively generic since they only affect the speed of growth, but not the end result of the growth process itself. In the future, however, we will use these two parameters to calibrate our model against long-term chronic studies.

4.1 Cardiac hypertrophy in systemic hypertension

Our first example illustrates the performance of the growth algorithm in the context of systemic hypertension. To mimic the effect of an increased systemic resistance, we increase the left ventricular pressure, while the right ventricular pressure remains at its baseline value, i.e., $p_{\text{LV}} > 100\,\text{mmHg}$ and $p_{\text{RV}} = 20\,\text{mmHg}$, respectively. The linear pressure increase toward these values, its constant plateau, and its linear decrease are documented in Fig. 6. In addition, Fig. 6 displays the normalized increase in cardiac mass. In response to pressure overload, the left ventricular wall thickens and the mass of the heart increases by approximately 52%. This increase in mass agrees favorably with the mass increase

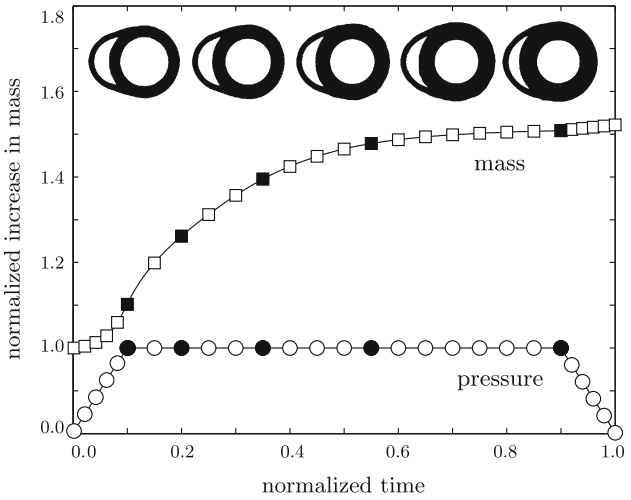

Fig. 6 Systemic hypertension. Temporal evolution of normalized applied pressure and normalized mass. An elevated left ventricular pressure induces a progressive left ventricular wall thickening accompanied by an increase in cardiac mass. Convergence is obtained at a mass increase of approximately 52%. At this point, the left ventricular wall has grown thick enough to withstand the elevated pressure level. The five sketched cross sections correspond to the five *black symbols* in the pressure and mass curves

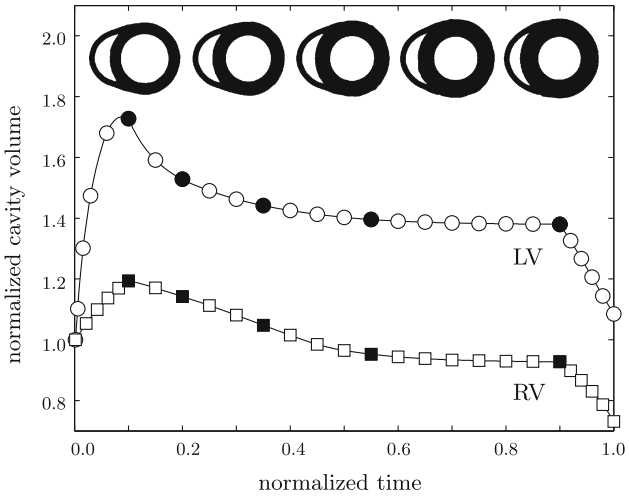

Fig. 7 Systemic hypertension. Temporal evolution of normalized left and right cavity volume. Acutely, the left ventricular cavity volume increases in response to left ventricular pressure overload. Chronically, due to progressive left ventricular wall thickening in response to pressure overload, the left ventricular cavity volume decreases progressively. At the same time, the left ventricle pushes into the right ventricle and its cavity volume decreases accordingly. The five sketched cross sections correspond to the five *black symbols* in the normalized cavity volume curves

reported in the literature from an initial value of 300–350 g to more than 500 g in response to severe systemic hypertension (Kumar et al. 2005). The mass increase decays over time until convergence is obtained. At that point, the ventricular wall has grown strong enough to pump against the elevated blood pressure. Figure 7 illustrates the temporal evolution of the normalized left and right cavity volume. Both increase initially as the pressure load is increased. Then, at constant pressure, the left ventricular wall begins to thicken in response to pressure overload. Accordingly, the left ventricular cavity volume decreases. The marked concentric thickening of the left ventricular wall associated with a significant reduction in lumen size agrees well with the pathophysiology of systemic hypertension (Kumar et al. 2005). As the wall thickens, it pushes into the right ventricle and induces a shrinkage of the right ventricular cavity volume.

Figure 8 displays the spatio-temporal evolution of the growth multiplier projected onto the adaptively grown heart. The five snapshots correspond to the five black symbols in Figs. 6 and 7. Overall, systemic hypertension manifests itself in left ventricular muscle thickening in an attempt to handle the higher left ventricular pressure. As such, left ventricular wall thickening is conceptually similar to wall thickening in arteries driven by hypertension (Kuhl et al. 2007). However, the complex geometry of the heart, in combination with its anisotropic microstructure, induces a heterogeneous stress profile which, in turn, triggers a heterogeneous progression of growth. The growth multiplier increases gradually from $\vartheta = 1.00$ to $\vartheta = 2.00$ as the individual cardiomyocytes of the left ventricle grow concentrically due to parallel sarcomere deposition. This is in quantitative agreement with a reported doubling of the cardiomyocyte diameter from approximately from 15 µm up to 40 µm (Opie 2003; Kumar et al. 2005). The growth process is initiated in the endocardium and progresses outward toward the epicardium until the entire left ventricular wall has grown from an initial value of 1.2 cm to a converged value of 2.4 cm. These values are in excellent quantitative agreement with the reported values of hypertrophic left ventricular wall thicknesses between 2.0 and 3.0 cm (Kumar et al. 2005; Maron and McKenna 2003). The right ventricle and the apex, however, are unaffected by the growth process and maintain their original thicknesses. In summary, the simulation illustrated in Fig. 8 is in excellent qualitative and quantitative agreement with the pathophysiological characteristics of systemic hypertension: progressive left ventricular wall thickening, increase in cardiac mass, and decrease in left ventricular cavity volume. Under chronic conditions, these geometric changes might eventually impair diastolic filling, reduce cardiac output, and decrease the overall blood supply to the body.

4.2 Cardiac hypertrophy in pulmonary hypertension

The second example illustrates the performance of the growth algorithm in pulmonary hypertension. Increased pulmonary resistance is modeled by increasing the right ventricular pressure while the left ventricular pressure remains at its baseline

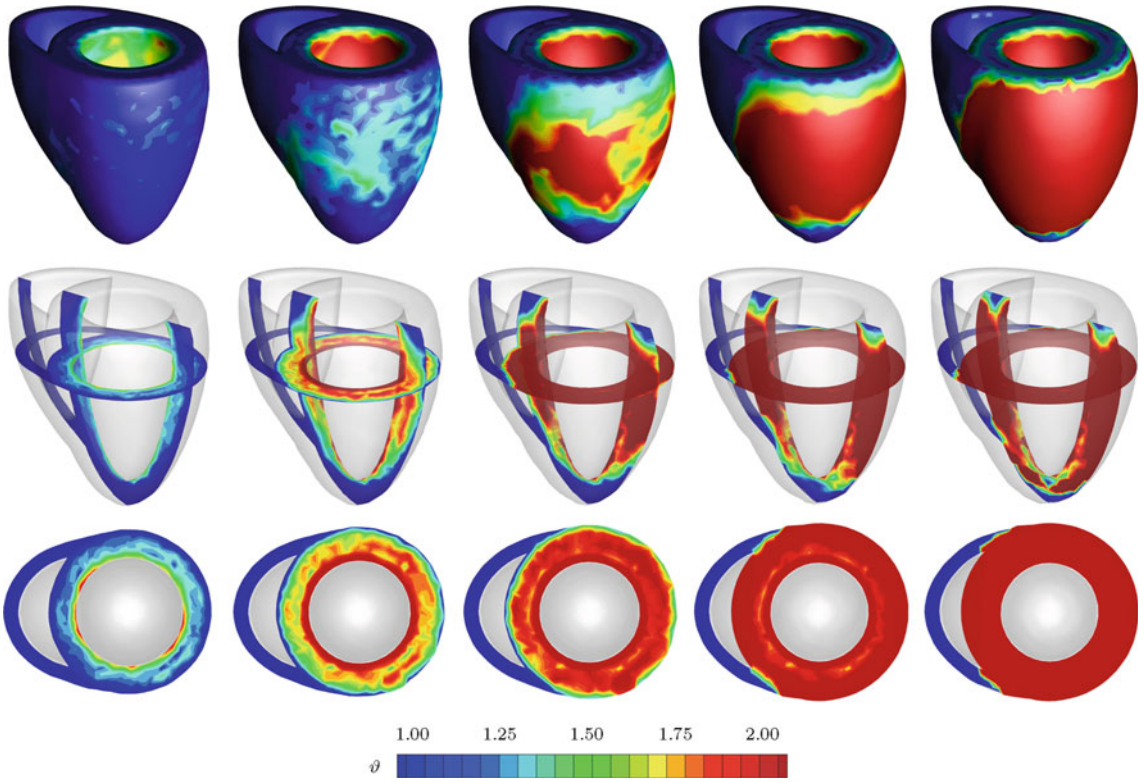

Fig. 8 Systemic hypertension. Spatio-temporal evolution of grown configuration and growth multiplier. On the macroscopic scale, systemic hypertension manifests itself in a progressive transmural left ventricular wall thickening to enable the left ventricle to pump against higher pressure levels. The right ventricle remains virtually unaffected. On the microscopic scale, left ventricular cardiomyocytes grow concentrically as the growth multiplier ϑ increases gradually from 1.00 to 2.00, while right ventricular cardiomyocytes maintain their normal shape. The five snapshots correspond to the five *black symbols* in Figs. 6 and 7

value, i.e., $p_{\mathrm{LV}} = 100\,\mathrm{mmHg}$ and $p_{\mathrm{RV}} > 20\,\mathrm{mmHg}$, respectively. In addition to the temporal evolution of the prescribed pressure loading, Fig. 9 shows the normalized increase in cardiac mass. In response to pressure overload, the cardiac mass increases as the right ventricular wall thickens. At a converged mass increase of approximately 10%, the right ventricular wall has grown thick enough to withstand the elevated pressure level. For this model, it seems that the overall mass increase in response to pulmonary hypertension is smaller than the mass increase in response to systemic hypertension. Figure 10 shows the temporal evolution of both cavity volumes. In contrast to the previous example, the left ventricular cavity volume now remains constant once the full pressure level is applied, while the right ventricular cavity volume decreases initially and then converges toward a plateau value. Similar to the previous example, pressure-overload-induced wall thickening is responsible for the reduction in right ventricular cavity volume. Finally, Fig. 11 documents the spatio-temporal evolution of the growth multiplier in pulmonary hypertension. Again, the depicted snapshots correspond to the five black symbols in Figs. 9 and 10. Acute pulmonary hypertension is characterized through a marked dilation of the right ventricle, initially without hypertrophy, see Fig. 11, left column. In agreement with pathological observations, in the cross-sectional view, Fig. 11, bottom row, the normal crescent shape of the right ventricle is transformed to a dilated ovoid (Voelkel et al. 2006). The dilation of the right ventricle shifts the interventricular septum toward the left ventricle, squeezing the left ventricle into its characteristic D-shaped form (Haddad et al. 2008). As a chronic consequence of pulmonary hypertension, the right ventricular wall begins to thicken. Similar to the previous example, the progression of growth is heterogeneous across the ventricle driven by a heterogeneous stress profile caused by microstructural anisotropy. In an attempt to maintain right ventricular wall stresses at a physiological level, the growth multiplier increases gradually from $\vartheta = 1.00$ to $\vartheta = 2.00$ as the individual cardiomyocytes of the right ventricle grow concentrically due to parallel sarcomere deposition. Convergence is obtained at a wall thickness of 1.2 cm, which agrees favorably with right ventricular wall thicknesses of more than 1.0 cm reported in the literature (Kumar et al. 2005). Although the left ventricle undergoes changes in shape which might significantly impair

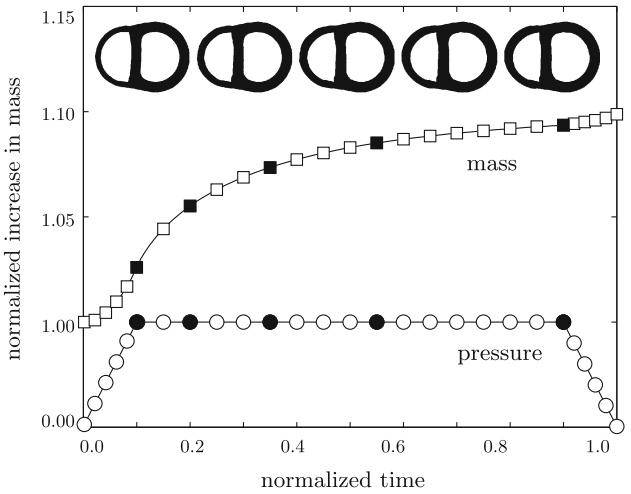

Fig. 9 Pulmonary hypertension. Temporal evolution of normalized applied pressure and normalized mass. An elevated right ventricular pressure induces a progressive right ventricular wall thickening accompanied by an increase in cardiac mass. Convergence is obtained at a mass increase of approximately 10%. At this point, the right ventricular wall has grown thick enough to withstand the elevated pressure level. The five sketched cross sections correspond to the five *black symbols* in the pressure and mass curves

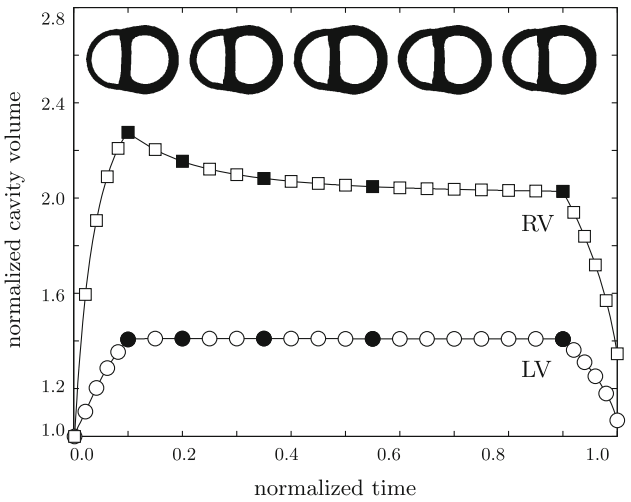

Fig. 10 Pulmonary hypertension. Temporal evolution of normalized right and left cavity volume. Acutely, the right ventricular cavity volume increases drastically in response to pressure overload. Chronically, the right cavity volume decreases slightly due to progressive right ventricular wall thickening in response to right ventricular pressure overload, while the left ventricular cavity volume remains virtually unaffected. The five sketched cross sections correspond to the five *black symbols* in the normalized cavity volume curves

its distensibility, preload, and elastance, its wall thickness remains virtually unaffected by the growth process. In summary, the simulation illustrated in Fig. 11 is in excellent agreement with the pathophysiological observations in pulmonary hypertension, both acutely and chronically: dilation of the right ventricle associated with cross-sectional shape changes from crescent shaped to oval, flattening of the interventricular septum, lateral compression of the left ventricle associated with cross-sectional shape changes from circular to D-shaped, progressive right ventricular wall thickening, and increase in cardiac mass. Under chronic conditions, these geometric changes may induce abnormal septal function, and impair left ventricular performance through ventricular interdependence.

5 Discussion

Similar to many other organs, the heart is known to adapt to changes in mechanical loading. When exposed to chronically elevated pressure levels, it is capable of increasing its wall thickness in an attempt to maintain wall stresses at their physiological levels. Hypertrophic wall thickening is a pathological adaptation of the heart muscle that is usually progressive and irreversible. Although the mechanical origins of wall thickening are similar under systemic and pulmonary hypertension, their pathophysiologies may be significantly different. Systemic hypertension primarily increases the thickness of the left ventricular wall with potentially unfavorable consequences of insufficient blood supply and impaired filling due to an increased wall stiffness. Pulmonary hypertension increases the thickness of the right ventricular wall, but in addition, it induces significant changes in cardiac geometry by pushing the septal wall into the left ventricle which might severely impair left ventricular performance and overall cardiac function. Neither systemic nor pulmonary hypertension are local conditions that affect only one side of the heart and their overall pathophysiology is typically characterized through ventricular interdependence.

In this manuscript, we have presented a methodology to explain and predict acute and chronic changes in cardiac form and function in response to hypertension using the field theories of continuum mechanics. We have adopted the concept of finite growth based on the introduction of an incompatible growth configuration introducing the multiplicative decomposition of the deformation gradient into an elastic and a growth part. For the growth part, we have proposed a micromechanically motivated definition, characterizing growth through a single scalar growth multiplier. For its evolution, we have suggested a stress-driven evolution equation governed by four material parameters. Since this evolution equation is motivated by observations on the molecular and cellular levels, its parameters have a clear biochemical interpretation. In particular, we model growth as the parallel addition of sarcomeres inside a cardiomyocyte, which thereby increases its cross-sectional area. The scalar growth multiplier of our model is therefore directly correlated with the number of sarcomere units within each

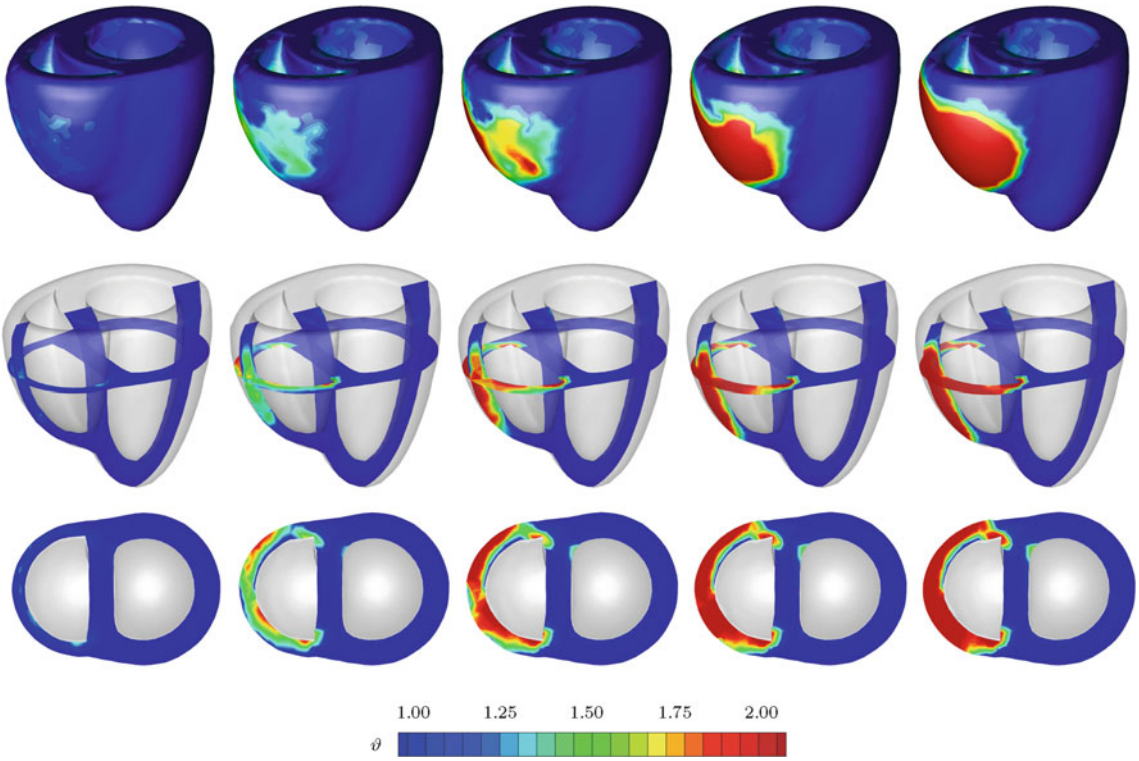

Fig. 11 Pulmonary hypertension. Spatio-temporal evolution of grown configuration and growth multiplier. On the macroscopic scale, acute pulmonary hypertension manifests itself in a significant enlargement of the right ventricle associated with a flattening of the interventricular septum and a compressed D-shaped left ventricle, left column. Chronic pulmonary hypertension initiates a progressive transmural right ventricular wall thickening, from left to right, to enable the right ventricle to pump against higher pressure levels. On the microscopic scale, right ventricular cardiomyocytes grow concentrically as the growth multiplier ϑ increases gradually from 1.00 to 2.00, while left ventricular cardiomyocytes maintain their normal shape. The five snapshots correspond to the five *black symbols* in Figs. 9 and 10

cell, and, accordingly, with the cross-sectional area of the cells themselves. Through locally varying fiber and sheet angles, cellular growth can have a different impact at different locations in the heart. We have combined the underlying approach with a recently proposed locally orthotropic model for cardiac muscle tissue and embedded the overall constitutive formulation in a geometrically nonlinear finite element setting with the growth multiplier treated as an internal variable on the integration point level. For its advancement in time, we have proposed an implicit Euler backward time integration scheme. To integrate the solution of the governing equations in an incremental iterative Newton-Raphson scheme, we have performed the consistent linearization of the underlying equations in their Eulerian format. We have demonstrated the performance of the proposed growth model in systemic and pulmonary hypertension using a generic biventricular heart geometry. The simulation has shown an excellent agreement with the pathophysiologies of acute and chronic left and right ventricular pressure overload capturing the characteristic changes in cardiac form and function.

The proposed model is, of course, a significant simplification of the complex pathways of systemic and pulmonary hypertension. It is based on the key assumption that molecular, cellular, and tissue level growth are affine. Since cardiomyocytes comprise more than three-fourths of the cardiac tissue volume, we believe that this is a reasonable first approximation but plan to explore the incorporation of different mechanisms for growth such as cardiomyocyte disarray in the near future. In the present model, growth is assumed to be driven by the trace of the overall stress tensor, i.e., by the pressure generated by both passive and active stresses. We are currently investigating different driving forces for hypertrophic growth such as the overall fiber stress or the active fiber stress which might be physiologically more realistic candidates to govern the growth process. In addition, it would be interesting to correlate the active stress with the electrical excitation (Göktepe and Kuhl 2009; Göktepe et al. 2010d; Kotikanyadanam et al. 2010) to study how pathological growth might impair the conduction system of the heart. Finally, one of the most exciting challenges is, of course, the calibration of the growth parameters in patient-specific geometries. Along these lines, global metrics of cardiac function such as end diastolic and end systolic left ventricular volumes, stroke volume, and ejection fraction could be extracted from the simulation and compared to clinically measured

patient data to calibrate and validate the model. We believe that, ultimately, this model has the potential to predict individual pathophysiologies in an attempt to design and optimize personalized treatment strategies.

Acknowledgments This material is based on work supported by the National Science Foundation CAREER award CMMI-0952021 "The Virtual Heart— Exploring the structure-function relationship in electroactive cardiac tissue", by the Hellman Faculty Scholars grant "A predictive multiscale simulation tool for heart failure", by the National Science Foundation ERFI program through grant EFRI-CBE-0735551 "Engineering of cardiovascular cellular interfaces and tissue constructs", and by the Stanford ARTS Fellowship.

References

Alastrue V, Martinez MA, Doblare M (2009) Modelling adaptative volumetric finite growth in patient-specific residually tressed arteries. J Biomech 41:1773–1781

Ambrosi D, Mollica F (2002) On the mechanics of a growing tumor. Int J Eng Sci 40:1297–1316

Ben Amar M, Goriely A (2005) Growth and instability in elastic tissues. J Mech Phys Solids 53:2284–2319

Berne RM, Levy MN (2001) Cardiovascular Physiology. The Mosby Monograph Series

Böl M, Reese S, Parker KK, Kuhl E (2009) Computational modeling of muscular thin films for cardiac repair. Comp Mech 43:535–544

Dokos S, Smaill BH, Young AA, LeGrice IJ (2002) Shear properties of passive ventricular myocardium. Am J Physiol Heart Circ Physiol 283:H2650–H2659

Emmanouilides GC, Riemenschneider RA, Allen HD, Gutgesell HP (1994) Moss and Adams' heart disease in infants, children, and adolescents, 5th edn. Lippincott Williams & Wilkins, Pennsylvania

Epstein M, Maugin GA (2000) Thermomechanics of volumetric growth in uniform bodies. Int J Plast 16:951–978

Garikipati K, Arruda EM, Grosh K, Narayanan H, Calve S (2004) A continuum treatment of growth in biological tissue: The coupling of mass transport and mechanics. J Mech Phys Solids 52:1595–1625

Garikipati K (2009) The kinematics of biological growth. Appl Mech Rev 62:030801-1–030801-7

Gerdes AM, Kellerman SE, Moore JA, Muffly KE, Clark LC, Reaves PY, Malec KB, Mc Keown PP, Schocken DD (1992) Structural remodeling of cardiac myocytes in patients with ischemic cardiomyopathy. Circulation 86:426–430

Göktepe S, Kuhl E (2009) Computational modeling of cardiac electrophysiology: a novel finite element approach. Int J Num Meth Eng 79:156–178

Göktepe S, Kuhl E (2010a) Electromechanics of cardiac tissue: a unified approach to the fully coupled excitation-contraction problem. Comp Mech 45:227–243

Göktepe S, Acharya SNS, Wong J, Kuhl E (2010b) Computational modeling of passive myocardium. Int J Num Meth Biomed Eng. doi:10.1002/cnm.1402

Göktepe S, Abilez OJ, Parker KK, Kuhl E (2010c) A multiscale model for eccentric and concentric cardiac growth through sarcomerogenesis. J Theor Bio 265:433–442

Göktepe S, Abilez OJ, Kuhl E (2010d) A generic approach towards finite growth with examples of athlete's heart, cardiac dilation, and cardiac wall thickening. J Mech Phys Solids 58:1661–1680

Göktepe S, Wong J, Kuhl E (2010e) Atrial and ventricular fibrillation: computational simulation of spiral waves in cardiac tissue. Arch Appl Mech 80:569–580

Guccione JM, McCulloch AD (1993) Mechanics of active contraction in cardiac muscle: Part I. Constitutive relations for active fiber stress that describe deactiveation. J Biomech Eng 115:72–81

Guccione JM, Moonly SM, Moustakidis P, Costa KD, Moutlon MJ, Ratcliffe MB, Pasque MK (2001) Mechanism underlying mechanical dysfunction in the border zone of left ventricular aneurysms: a finite element study. Ann Thorac Surg 71:654–662

Haddad F, Doyle R, Murphy DJ, Hunt SA (2008) Right ventricular function in cardiovascular disease. Part II. Pathophysiology, clinical importance, and management of right ventricular failure. Circulation 117:1717–1731

Han MK, McLaughlin VV, Criner GJ, Martinez FJ (2007) Pulmonary diseases and the heart. Circulation 116:2992–3005

Harrington KB, Rodriguez F, Cheng A, Langer F, Ashikaga H, Daughters GT, Criscione JC, Ingels NB, Miller DC (2005) Direct measurement of transmural laminar architecture in the anterolateral wall of the ovine left ventricle: new implications for wall thickening mechanisms. Am J Physiol Heart Circ Physiol 228:H1324–H1330

Himpel G, Kuhl E, Menzel A, Steinmann P (2005) Computational modeling of isotropic multiplicative growth. Comp Mod Eng Sci 8:119–134

Himpel G, Menzel A, Kuhl E, Steinmann P (2008) Time-dependent fibre reorientation of transversely isotropic continua—finite element formulation and consistent linearization. Int J Num Meth Eng 73:1413–1433

Holzapfel GA, Ogden RW (2009) Constitutive modelling of passive myocardium. A structurally-based framework for material characterization. Phil Trans R Soc London A 367:3445–3475

Humphrey JD (2008) Vascular adaptation and mechanical homeostasis at tissue, cellular, and sub-cellular levels. Cell Biochem Biophys 50:53–78

Humphrey JD, Rajagopal KR (2002) A constrained mixture model for growth and remodeling of soft tissues. Math Mod Meth Appl Sci 12:407–430

Hunter JJ, Chien KR (1999) Signaling pathways for cardiac hypertrophy and failure. New England J Med 341:1276–1283

Itoh A, Krishnamurthy G, Swanson J, Ennis D, Bothe W, Kuhl E, Karlsson M, Davis L, Miller DC, Ingels NB (2009) Active stiffening of mitral valve leaflets in the beating heart. Am J Physiol Heart Circ Physiol 296:1766–1773

Kotikanyadanam M, Göktepe S, Kuhl E (2010) Computational modeling of electrocardiograms: a finite element approach towards cardiac excitation. Int J Num Meth Biomed Eng 26:524–533

Krishnamurthy G, Itoh A, Swanson J, Bothe W, Karlsson M, Kuhl E, Miller DC, Ingels NB (2009) Regional stiffening of the mitral valve anterior leaflet in the beating heart. J Biomech 42:2697–2701

Kroon W, Delhaas T, Arts T, Bovendeerd P (2009) Computational modeling of volumetric soft tissue growth: application to the cardiac left ventricle. Biomech Model Mechanobio 8:309–310

Kuhl E, Steinmann P (2003) Mass- and volume specific views on thermodynamics for open systems. Proc Royal Soc 459:2547–2568

Kuhl E, Steinmann P (2003) On spatial and material settings of thermohyperelstodynamics for open systems. Acta Mech 160:179–217

Kuhl E, Menzel A, Steinmann P (2003) Computational modeling of growth—a critical review, a classification of concepts and two new consistent approaches. Comp Mech 32:71–88

Kuhl E, Garikipati K, Arruda EM, Grosh K (2005) Remodeling of biological tissue: mechanically induced reorientation of a transversely isotropic chain network. J Mech Phys Solids 53:1552–1573

Kuhl E, Holzapfel GA (2007) A continuum model for remodeling in living structures. J Mat Sci 2:8811–8823

Kuhl E, Maas R, Himpel G, Menzel A (2007) Computational modeling of arterial wall growth: attempts towards patient-specific simulations based on computer tomography. Biomech Mod Mechanobio 6:321–331

Kumar V, Abbas AK, Fausto N (2005) Robbins and Cotran pathologic basis of disease. Elsevier Saunders, Amsterdam

Lee EH (1969) Elastic-plastic deformation at finite strains. J Appl Mech 36:1–6

Libby P, Bonow RO, Mann DL, Zipes DP (2007) Braunwald's heart disease. Saunders, Philadeiphia

Lubarda A, Hoger A (2002) On the mechanics of solids with a growing mass. Int J Solids Struct 39:4627–4664

Maron BJ, McKenna WJ (2003) American college of cardiology/European society of cardiology: clinical expert consensus document on hypertrophy cardiomyopathy. J Am College Cardiol 42:1687–1713

Menzel A (2005) Modelling of anisotropic growth in biological tissues—A new approach and computational aspects. Biomech Model Mechanobiol 3:147–171

Opie LH (2003) Heart physiology: from cell to circulation. Lippincott Williams & Wilkins, Pennsylvania

Rodriguez EK, Hoger A, McCulloch AD (1994) Stress-dependent finite growth in soft elastic tissues. J Biomech 27:455–467

Russel B, Curtis MW, Koshman YE, Samarel AM (2010) Mechanical stress-induced sarcomere assembly for cardiac muscle growth in length and width. J Mol Cell Card 48:817–823

Sawada K, Kawamura K (1991) Architecture of myocardial cells in human cardiac ventricles with concentric and eccentric hypertrophy as demonstrated by quantitative scanning electron microscopy. Heart Vessels 6:129–142

Schmid H, Pauli L, Paulus A, Kuhl E, Itskov M (2010) How to utilise the kinematic constraint of incompressibility for modelling adaptation of soft tissues. Comp Meth Biomech Biomed Eng, accepted for publication

Taber LA (1995) Biomechanics of growth, remodeling and morphogenesis. Appl Mech Rev 48:487–545

Taber LA, Humphrey JD (2001) Stress-modulated growth, residual stress, and vascular heterogeneity. J Biomech Eng 123:528–535

Voelkel NF, Quaife RA, Leinwand LA, Barst RJ, McGoon MD, Meldrum DR, Dupuis J, Long CS, Rubin LJ, Smart FW, Suzuki YJ, Gladwin M, Denholm EM, Gail DB (2006) Right ventricular function and failure. Report of a National Heart, Lung, and Blood Institute Working Group on Cellular and Molecular Mechanisms of Right Heart Failure. Circulation 114:1883–1891

Weitzenblum E (2003) Chronic cor pulmonale. Heart 89:225–230

Yin FC, Chan CC, Judd RM (1996) Compressibility of perfused passive myocardium. Am J Physiol Heart Circ Physiol 271:H1864–H1870

Yoshida M, Sho E, Nanjo H, Takahashi M, Kobayashi M, Kawamura K, Honma M, Komatsu M, Sugita A, Yamauchi M, Hosoi T, Ito Y, Masuda H (2010) Weaving hypothesis of cardiomyocyte sarcomeres. Am J Pathol 176:660–678